Recent increases in tropical cyclone precipitation extremes over the US east coast

Justin T. Maxwell[a,1], Joshua C. Bregy[a,b], Scott M. Robeson[a], Paul A. Knapp[c], Peter T. Soulé[d], and Valerie Trouet[e]

[a]Department of Geography, Indiana University Bloomington, Bloomington, IN 47405; [b]Department of Earth and Atmospheric Sciences, Indiana University Bloomington, Bloomington, IN 47405; [c]Department of Geography, Environment, and Sustainability, University of North Carolina at Greensboro, Greensboro, NC 27402; [d]Department of Geography and Planning, Appalachian State University, Boone, NC 28608; and [e]Laboratory of Tree-Ring Research, University of Arizona, Tucson, AZ 85721

Edited by Zhisheng An, Institute of Earth Environment, Chinese Academy of Sciences, Xi'an, China, and approved August 20, 2021 (received for review March 23, 2021)

The impacts of inland flooding caused by tropical cyclones (TCs), including loss of life, infrastructure disruption, and alteration of natural landscapes, have increased over recent decades. While these impacts are well documented, changes in TC precipitation extremes—the proximate cause of such inland flooding—have been more difficult to detect. Here, we present a latewood tree-ring–based record of seasonal (June 1 through October 15) TC precipitation sums (ΣTCP) from the region in North America that receives the most ΣTCP: coastal North and South Carolina. Our 319-y-long ΣTCP reconstruction reveals that ΣTCP extremes (≥0.95 quantile) have increased by 2 to 4 mm/decade since 1700 CE, with most of the increase occurring in the last 60 y. Consistent with the hypothesis that TCs are moving slower under anthropogenic climate change, we show that seasonal ΣTCP along the US East Coast are positively related to seasonal average TC duration and TC translation speed.

tropical cyclones | tree rings | translation speed | extreme precipitation

Landfalling tropical cyclones (TCs) produce high winds, storm surges, and inland flooding that can have devastating impacts on human and natural landscapes (1). TC-related flooding can cause billions of dollars in structural damage (2) and is one of the deadliest aspects of TCs (3, 4). Moreover, climate model simulations suggest that TCs produce more precipitation under anthropogenic forcing, particularly within the center of the TCs (5–9). However, our understanding of the impacts and potential trends in the flood hazard caused by excess precipitation from TCs in the United States is limited by the length of the instrumental TC precipitation (TCP) record (1948 to present) (10).

Along the US east coast—an area considered to have the most complete record of TCs through time worldwide (11–13)—the translation speed of TCs has decreased in recent decades (14), which could result in higher TCP totals (ΣTCP) (15). This slowdown is in line with global decreases in translation speed by 10% from 1949 to 2016 (16) and has been implicitly related to the weaker global wind circulation from anthropogenic warming (17, 18). However, part of this slowing of TC speed is an artifact of the introduction of satellite data recording a larger number of weaker and smaller TCs, biasing the record of TC translation speed (19–21). To place modern changes in TC characteristics—and this recent slowdown—in a historical perspective and to investigate potential links to anthropogenic climate change, long-term (i.e., multicentury) records are needed. Slower TCs produce more TCP (15), and long-term trends in ΣTCP could therefore provide further evidence that TCs are slowing.

Reliable detection of changes in ΣTCP, however, has proven challenging and therefore produced mixed results. Annual ΣTCP in the United States (10, 22) and globally (23) show no significant trends over the observed record. Yet, studies that focus on TCP amounts from individual storms have found increases in 1) TC-induced "drought-busting" events (24, 25), 2) TC-associated heavy rainfall events (26), and 3) Individual storm-related TCP amounts in US coastal cities (15). This inconsistency can be explained by the substantial interannual variability within the short instrumental TCP record, which limits our ability to reliably detect changes in ΣTCP through time.

Here, we use 300+ years of tree-ring data to extend the record of seasonal (June 1 to October 15; *Materials and Methods*) ΣTCP for the coast of North Carolina and South Carolina (Fig. 1). This region experiences the highest annual ΣTCP in North America (10), averaging ∼50 mm/year (1948 to 2018) and the highest contribution of ΣTCP to annual precipitation (up to 8%; Fig. 1 *A* and *B*). In many years, ΣTCP accumulates within a few days and can create widespread flooding. For instance, of the 5 y with the largest ΣTCP in this region, three were generated predominantly by a single storm that produced ΣTCP exceeding 200 mm (Fig. 1*C*). However, the 2 y with the largest ΣTCP were generated by multiple storms: Connie and Diane (190 and 110 mm) in 1955 and Bertha and Fran (110 mm and 175 mm) in 1996 (Fig. 1*C*).

To reconstruct seasonal ΣTCP and extend the ΣTCP record to 1700 CE, we use the latewood portion of tree rings from *Pinus palustris* Mill. (longleaf pine). Our reconstruction is based on tree-ring data collected from seven sites in North Carolina and South Carolina (Fig. 1), which allows the development of a regional ΣTCP reconstruction that is calibrated against a gridded dataset of ΣTCP: TCPDat (10). By creating a regional ΣTCP reconstruction, we expand upon earlier ΣTCP reconstruction work (27, 28) spatially as well as temporally. This allows us to determine spatiotemporal ΣTCP variability and in particular, whether extreme ΣTCP have increased over time, as is expected in a warmer world.

Significance

Using a tree-ring–based reconstruction of tropical cyclone precipitation summed over June 1 through October 15, we found that extremely high tropical cyclone precipitation amounts have increased over the past 300 years. By looking at other characteristics of tropical cyclones, we find that this increase is linked to the longer average duration of tropical cyclones. The extremes (≥0.95 quantile) of summed tropical cyclone precipitation have increased by 2 to 4 mm/decade since 1700, resulting in an increase of 64 to 128 mm compared to extremes in the early 1700s. This study documents increases in extremes of summed tropical cyclone precipitation, which provides another line of evidence that the speed of movement of tropical cyclones is slowing.

Author contributions: J.T.M., S.M.R., and V.T. designed research; J.T.M., J.C.B., S.M.R., P.A.K., and P.T.S. performed research; J.T.M., J.C.B., and S.M.R. analyzed data; and J.T.M. wrote the paper.

The authors declare no competing interest.

This article is a PNAS Direct Submission.

[1]To whom correspondence may be addressed. Email: maxweljt@indiana.edu.

This article contains supporting information online at https://www.pnas.org/lookup/suppl/doi:10.1073/pnas.2105636118/-/DCSupplemental.

Published October 4, 2021.

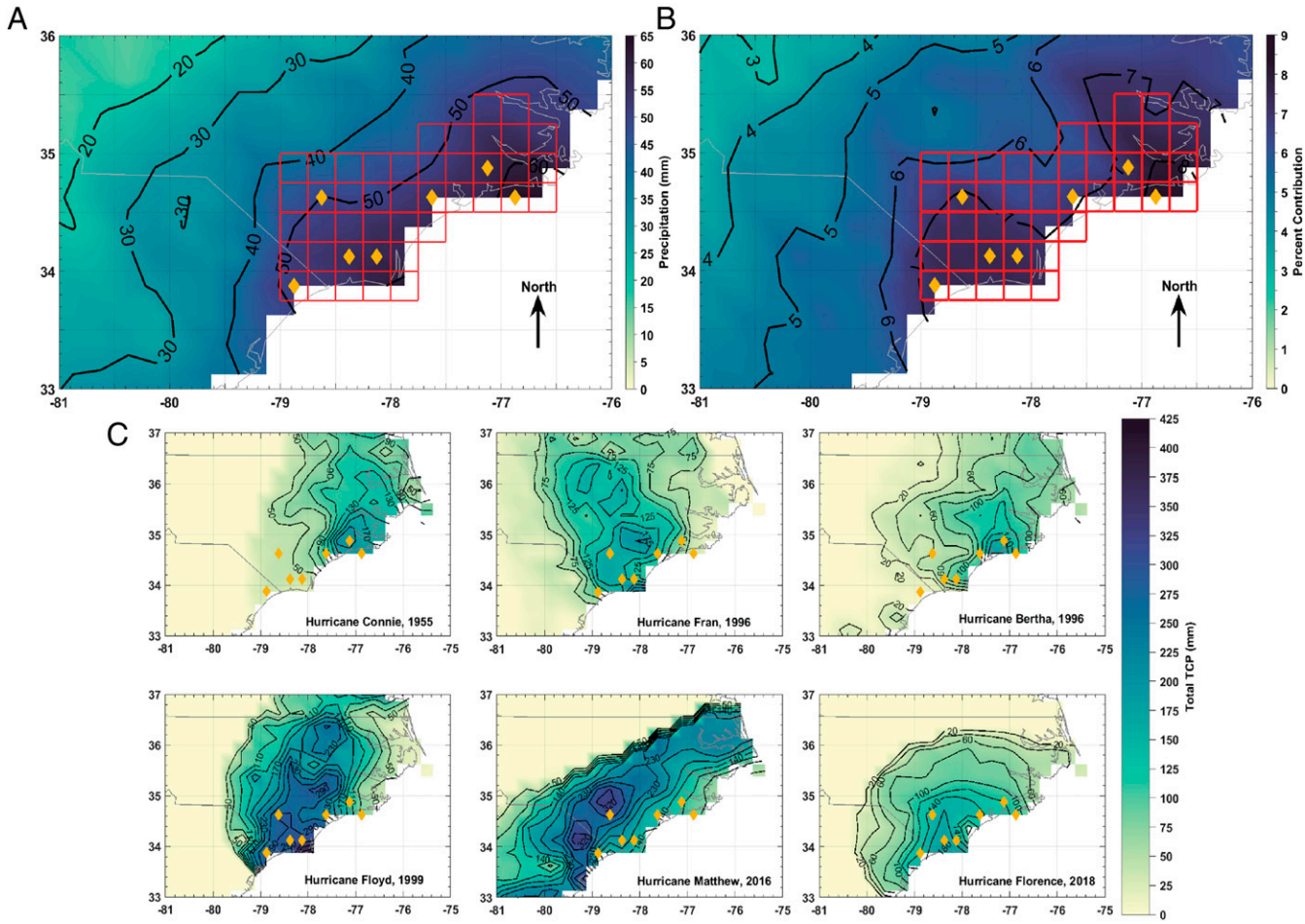

Fig. 1. Instrumental TCP seasonal and extreme year totals. Average (1948 through 2018) June 1 to October 15 ΣTCP (*A*) and seasonal average contribution of ΣTCP to overall precipitation (*B*) (1948 through 2018). Red squares represent the 0.25° grids where data were averaged to calculate the regional ΣTCP. (*C*) Maps of individual storms that had large ΣTCP (millimeters) over the instrumental record. Orange diamonds are tree-ring sites. Data for all plots were created from TCPDat (10).

Results

ΣTCP Reconstruction. All seven of the adjusted latewood (*Materials and Methods*) chronologies were significantly positively correlated with regional instrumental ΣTCP but, importantly, did not respond strongly to regional non-ΣTCP (*SI Appendix*, Table S1). These results support the hypothesis that late-season wood production (i.e., latewood width) responds primarily to the large, short-duration inputs of precipitation produced by TCs (27, 28). Due to different record lengths of the chronologies, the overall reconstruction model is composed of a series of nested principal-component reconstruction models (*Materials and Methods*) that explain between 34 and 41% of the variance in regional instrumental ΣTCP (*SI Appendix*, Fig. S1 and Table S2). After combining the nested models, our reconstruction spans 1700 through 2015 CE (*SI Appendix*, Table S2). The reconstruction overestimated low (1- to 40-mm) ΣTCP values and underestimated high (>100-mm) values, and we used a quantile-mapping bias-correction procedure (29) (*Materials and Methods*) to reduce these systematic differences (Fig. 2).

Increases in ΣTCP Extremes. Using quantile regression to estimate linear trends for the entire bias-corrected reconstruction (*Materials and Methods*), the upper tail (≥0.95 quantile) of ΣTCP shows a significant increase over time, whereas other quantiles exhibit either negative or nonsignificant trends (Fig. 3). This increasing trend starts at the 0.90 quantile (~1 mm/decade) with the 0.95 and greater quantiles (years with ΣTCP of at least 174 mm) showing stronger trends (~2 to 4mm/decade) (Fig. 3*B*). A total 6 of the 10 yrs with ΣTCP in the 0.95 quantile happened after the year 1900. Further, 5 of the 7 yrs of highest ΣTCP occurred in the late 20th/early 21st centuries (1955, 1996, 1999, 2016, and 2018). For years of extreme (≥0.95 quantile) ΣTCP in the 21st century, the estimated linear trend of 2 to 4 mm/decade translates into an increase of 64 to 128 mm compared to years of extreme ΣTCP in the early 1700s.

The trend in the reconstruction toward increasingly more extreme ΣTCP is supported by the instrumental record, which also shows its largest ΣTCP extremes (>300 mm) in more recent years (Fig. 2*A*). The two most recent years of extreme ΣTCP include 2016, with Tropical Storm Julia and Hurricane Matthew producing a combined 334 mm of TCP, and 2018, when Hurricane Florence produced 292 mm of TCP, causing $10.3 and $24.2 billion in damages, respectively (30, 31). We also examined whether the seasonal timing of TC occurrence differentially impacted latewood growth, potentially influencing the reliability of the reconstruction but found no significant differences in adjusted latewood growth between different months of TC occurrence (*SI Appendix*, Fig. S2).

Only in 2 yrs in the early to mid-18th century, 1703 and 1741, did extreme ΣTCP rival these recent extremes (Fig. 3*A*). These earlier extreme ΣTCP are unrelated to increased variance in the nested tree-ring models (*SI Appendix*, Fig. S3). Further, historical documents substantiate that a strong TC affected a large area of the East Coast from Virginia to Pennsylvania in October 1703

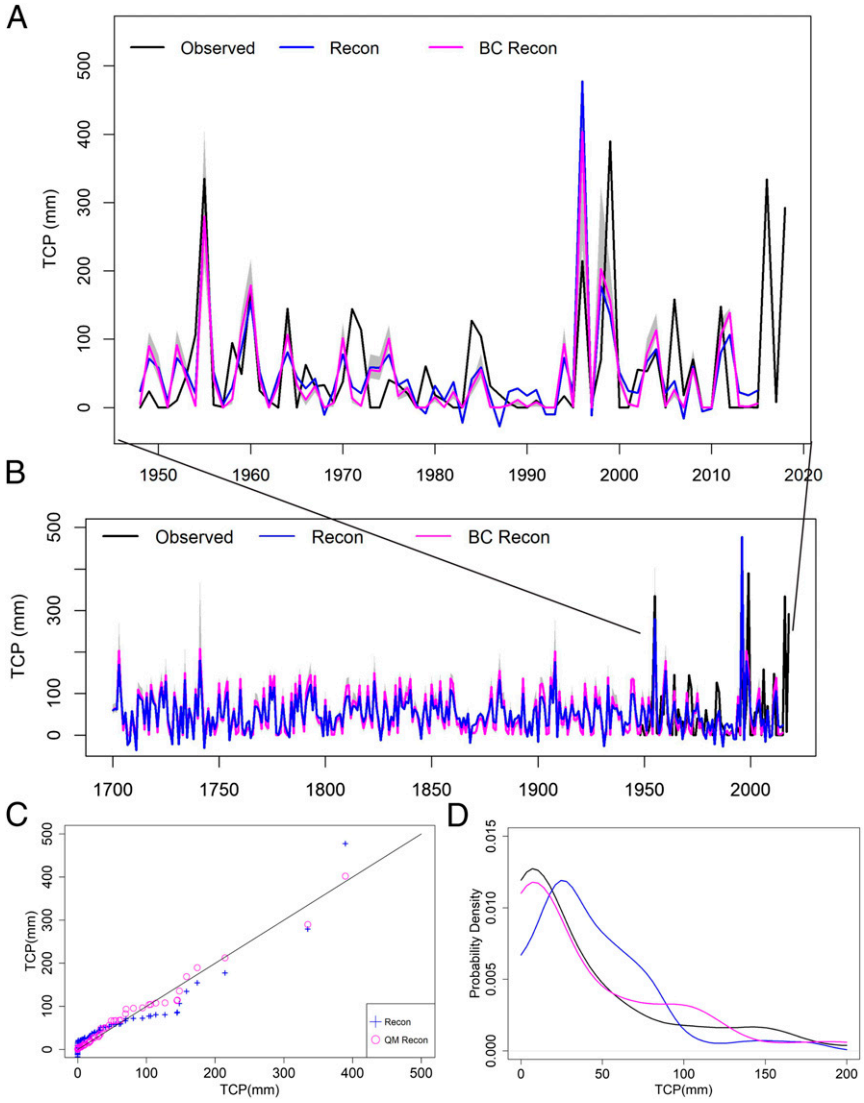

Fig. 2. Bias-corrected ΣTCP reconstruction. (*A*) Time series of a common period between observed uncorrected and bias-corrected (BC) ΣTCP from the most replicated model. (*B*) Time series of full reconstruction period of uncorrected reconstruction and bias-reconstructed along with observed ΣTCP record. The gray shading is the uncertainty in the reconstruction and represents inner 95% of the spread of the 999 bootstrapped ensembles. (*C*) A quantile–quantile plot between the uncorrected and bias-corrected reconstruction. (*D*) Kernel density estimates of the probability density functions for the observed, uncorrected, and bias-corrected reconstructions of ΣTCP, showing how the probability distribution of the uncorrected reconstruction differs from that of the observations.

(32). Our results suggest that TCP from this storm also affected the North Carolina and South Carolina coasts. Our reconstruction further suggests an undocumented storm (or multiple storms) in 1741 that affected the North Carolina and South Carolina coasts, a year currently without historical documentation of heavy rainfall or flooding from TCs, to the best of our knowledge.

Changes in TC Duration. ΣTCP in a given year can be influenced by the annual number of TCs that make landfall, the average duration of these TCs, and their translation speed. Therefore, an increase in ΣTCP extremes can indicate an increase in one or more of these factors. For our region, we found that instrumental (1948 to 2018) seasonal ΣTCP was significantly positively correlated with average ($r = 0.807$, $P < 0.01$) and summed ($r = 0.893$, $P < 0.01$) seasonal TC duration but negatively correlated with seasonal average TC translation speed ($\rho = -0.602$; $P < 0.01$; *SI Appendix*, Table S3). Correlations with these TC metrics were of the same sign and significant, albeit weaker, for our reconstructed ΣTCP over the instrumental period (*SI Appendix*, Table S3) and with the longer Hurricane Database (HURDAT2) dataset time period (1851 to 2018) (*SI Appendix*, Table S3; correlation with TC translation speed is not significant).

The relationship between ΣTCP with TC duration and TC translation speed, with a particular emphasis on extremes in both metrics, is further demonstrated by the results of our SEA analyses (Fig. 4 *D* and *E*). Years with extreme (≥0.95 quantile) average TC durations or TC translation speeds (HURDAT2; 1851 to 2018) are associated with significantly larger ΣTCP (Fig. 4*D*). Similarly, years with extreme (≥0.95 quantile) reconstructed ΣTCP are associated with significantly longer average TC durations and slower TC translation speeds (Fig. 4*E*). Our findings thus suggest that the TC slowdown in recent decades, expressed by lower TC translation speeds and longer durations, is an important control on the trend of increasing extreme ΣTCP.

While our findings support a relationship between ΣTCP and annually averaged TC duration and speed, we also find a relationship between ΣTCP and the number of TCs (*SI Appendix*, Table S3), making it difficult to determine whether the increases

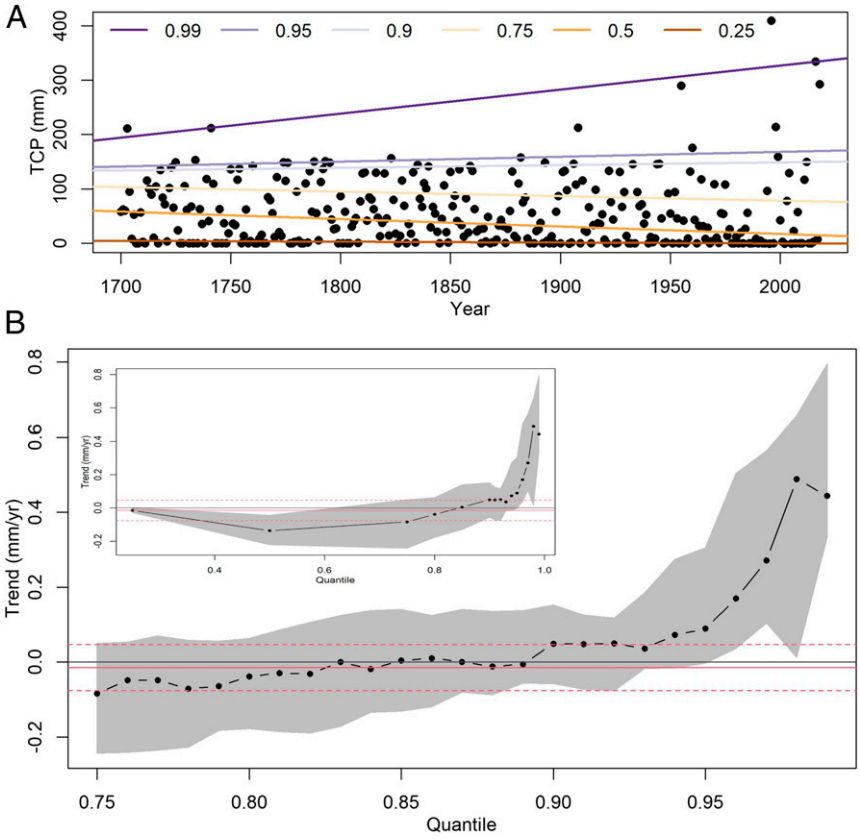

Fig. 3. Trends in reconstrcuted ΣTCP. (*A*) The ΣTCP reconstruction (1700 through 2015) combined with observed values (2016 through 2018) with quantile-based regression slopes for the 0.99, 0.95, 0.75, 0.50, and 0.25 quantiles. (*B*) Quantile-based trends for the upper end of the distribution (0.75 through 0.99; black dotted line) with 95% uncertainity estimates (gray shading). The solid red line represents the ordinary least squares trend (and the red dashed lines its 95% uncertainty estimates). The inset figure shows the trends for a wider range of quantiles, including the lower tail.

in ΣTCP extremes are due to increases in the number of TCs or slower TCs or both. However, we find that the number of TCs making landfall in our study region has not changed using Mann–Kendall trend test (−0.002 TCs per year; $\tau = -0.067$; $P = 0.8821$) since the start of the HURDAT2 (33) dataset in 1851, whereas their translation speed has decreased (−0.026 kn per year; $\tau = -0.137$; $P < 0.05$) and their average duration has increased significantly (0.01 h per year; $\tau = 0.093$; $P < 0.05$) (Fig. 4 *A*–*C*). To determine the role that the number of storms in a given year could have on our results, we examined storm-level statistics (*Materials and Methods*). We found a significant relationship ($\rho = -0.480$; $P < 0.01$; 1948 through 2018) between the translation speed per TC and the TCP per TC (*Materials and Methods*). We examined trends in TCP from TCs that have similar translation speeds (binned in groups of 5 kn) to further demonstrate the role of TC speeds on the increasing trend of ΣTCP extremes. In the three groups (5 to 9 kn, 10 to 14 kn, and 15 to 19 kn) that had a sufficiently large sample size (≥~20 TCs), TCP did not have a significant trend through time (*SI Appendix*, Fig. S4). However, if we examine TCP per TC from every storm from 1948 to 2018, there is a weak increasing trend ($\tau = 0.111$; $P = 0.08$; *SI Appendix*, Fig. S4). These results support that the TCP of a given storm is related to the speed of that TC and those speeds have been slowing through time (Fig. 4 *A* and *B*), resulting in larger extremes in ΣTCP.

While instrumental ΣTCP are weakly related to climatic drivers along the US Atlantic coast, particularly the Bermuda High and El Niño Southern Oscillation (ENSO) (10, 34), reconstructed ΣTCP have minimal to no connection to these climate drivers (*SI Appendix*, Table S3). Sea surface temperatures (SSTs) in the tropical and North Atlantic have increased in recent decades and have been linked to increased TC activity (35). However, ΣTCP were not significantly correlated with either gridded SSTs for any portion of the North Atlantic (1850 through 2016; Hadley Center) or with reconstructed western Atlantic tropical SSTs (36) (*SI Appendix*, Table S4), suggesting that it is unlikely that climatic/oceanic interactions are driving the increase in ΣTCP extremes.

Discussion

Climate model projections of future TC translation speeds and durations vary widely, and the contribution of anthropogenic climate change in the slowing of TCs is uncertain (37, 38). Our ΣTCP reconstruction indicates that ΣTCP have increased in their extremes, a change that is related to seasonal average TC duration and TC translation speed but not to increases in SSTs. Therefore, if TCs are more likely to slow down in a warming world, the increasing trend in extreme ΣTCP should continue, resulting in more TCP-related flooding. Further, a warmer climate has been shown to slow the decay of TCs after making landfall, indicating that areas farther inland will receive higher amounts of TCP (39) and increase the water vapor content, which is expected to increase TCP rates (5). TC storm tracks also have shifted westward globally, making landfalling TCs, and consequently higher ΣTCP, more likely for the US east coast (40, 41), even if this may be more complex at the oceanic basin level (42). The combination of these factors indicates that the future is likely to have increased extremes in ΣTCP, a pattern that our multicentennial reconstruction documents. Increased ΣTCP will influence water management, flood insurance claims, and water pollution through runoff

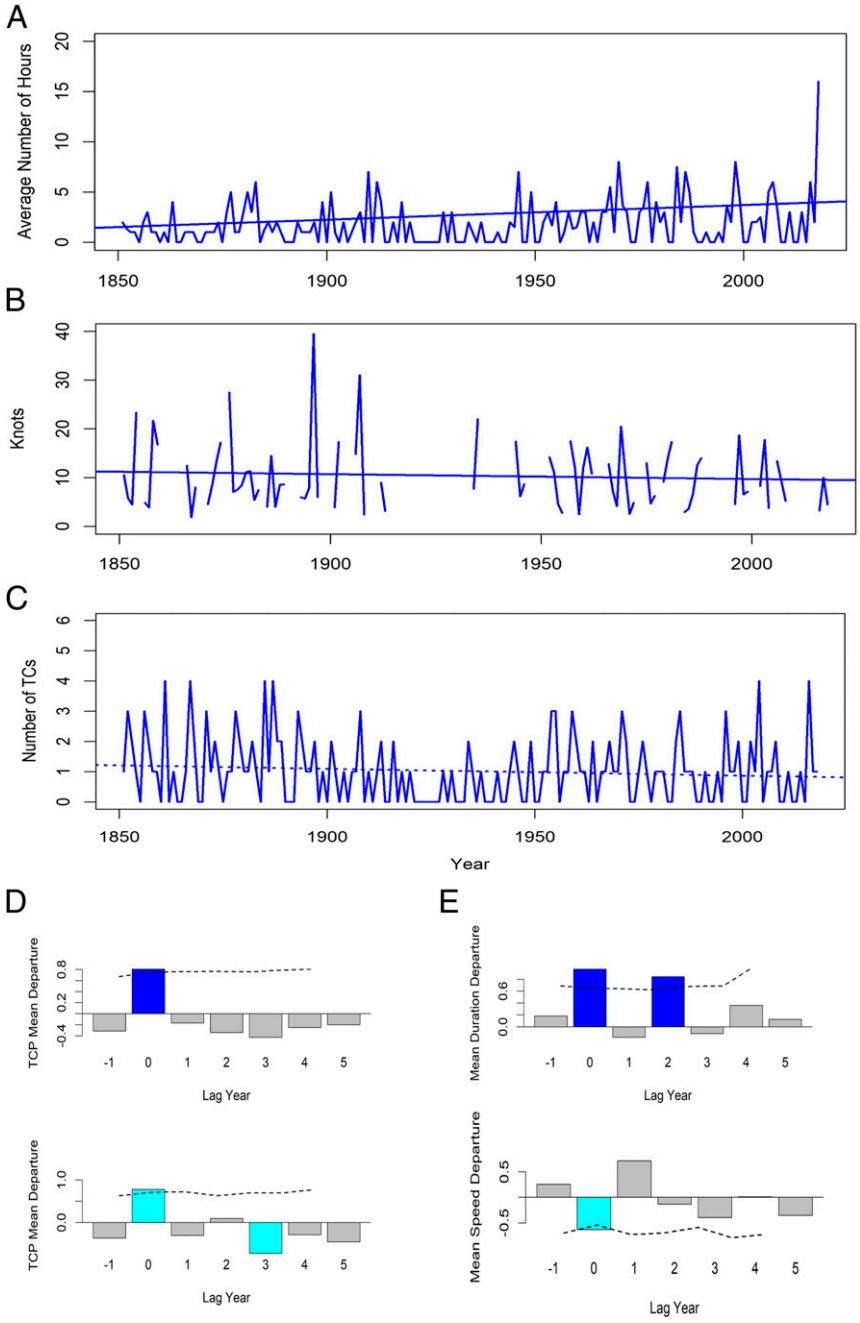

Fig. 4. Trends in TC duration, number, and speed. (*A*) Time series of the seasonal average TC duration (number of 6-h segments that a TC was within 223 km of the study region divided by the number of TCs for that year) with trend line. (*B*) Time series of average TC translation speed for the portions of the TC tracks that were within 223 km of the study region with trend line. Breaks in the line are due to years when no TCs were in the region and therefore are not available for speed. (*C*) Time series of the number of TCs that affected the study region with trend line. All the time series were derived from HURDAT2. Solid trend lines represent significant trends ($P < 0.05$), while the dashed line represents a nonsignificant trend. (*D*) SEA of ΣTCP reconstruction with seasonal average TC duration (*Top*; $n = 12$) and seasonal average TC translation speed (*Bottom*; $n = 11$). (*E*) SEA of seasonal average TC duration time series (*Top*) and seasonal average TC translation speed (*Bottom*) with years with extreme ΣTCP as event years ($n = 12$). Event years were selected based on years that were greater than the 95th quantile, except for seasonal average TC translation speed, which was the 90th quantile. Blue columns represent significant departures at $P < 0.01$, and cyan represents $P < 0.05$.

and ruptured waste lagoons (43) for coastal cities. As a result, warmer conditions will simultaneously increase water demand and evapotranspiration rates (44) while also leading to higher ΣTCP (and other high rainfall events) (45–47). Therefore, warmer conditions will likely cause increased interannual variability in droughts, flooding, and water availability in the coastal southeastern United States.

Materials and Methods

Instrumental ΣTCP Data. To generate seasonal ΣTCP, we used daily instrumental gridded (0.25° × 0.25°) TCP data from TCPDat (10) (1948 through 2018), which is a publicly available product (https://github.com/jbregy/TCPDat). TCPDat combines gridded precipitation data from the Climate Prediction Center (48) with the TC best track data from HURDAT2 (33, 49), available from the World Meteorological Organization's International Best Track Archive for Climate

Stewardship initiative version 03r09 (49). TCPDat provides robust spatial coverage of TCP allowing the observed record to not be dominated by a single weather station. While the hurricane season lasts officially from June 1 to November 30, most longleaf pine trees stop growing by October 15 (50). We therefore defined seasonal ΣTCP for each year as the sum of daily TCP for the period June 1 to October 15, the period best captured by latewood ring width (27). We created a regional (spatial) average of ΣTCP based on 43 contiguous grid points that received at least an average of 40 mm/year and ensured that every grid point that contained a tree-ring site was included (Fig. 1). We also calculated seasonal non-ΣTCP by subtracting the ΣTCP from seasonal total (June 1 to October 15) precipitation for each of the 43 grid points and then spatially averaging for each year.

Field and Laboratory Methods. We used five previously published latewood-width chronologies (27, 28) along with two newly sampled longleaf pine latewood width chronologies for a total of seven sites across North Carolina and South Carolina (Fig. 1). We further extended two of the previously published chronologies with remnant wood cross-section data (*SI Appendix*, Table S5). All seven sites are located on Carolina bay sand rims and support longleaf/wiregrass woodland communities. Seasonal ΣTCP in these sand rims, which rise 0.5 to 1.5 m above the surrounding area and drain water efficiently, account for approximately half of the variance in latewood growth from resident longleaf pine (27, 28). At each site, we targeted every canopy-dominant tree with old-growth morphology (13 to 36 trees per site). For each tree, we extracted two samples from opposite sides at ∼1.3 m above the ground. To extend the chronology, we also extracted cross-sections from stumps and remnant wood using a chainsaw.

We measured the earlywood, latewood, and total ring width using WinDendro (version 2017a) for all core samples and statistically cross-dated the samples using the program COFECHA (51). Similarly, we measured two transects for each cross-section. We detrended individual tree-ring time series to remove the biological growth trend and nonclimatic influences of growth (e.g., disturbance) by using a two-thirds spline (52) with the adjustment for endpoints (53) in the program ARSTAN (54). Fire is relatively infrequent at these sites compared to other pine savannas, but it is still part of the ecosystem. Thus, we used the two-thirds spline as the detrending method to maximize the retained climate signal and remove nonclimatic noise. Lastly, we created chronologies for each site using a biweight average of the individual series (i.e., core and cross-section measurements; *SI Appendix*, Table S5).

Adjusted Latewood. Climate and other environmental conditions in the early growing season influence latewood width in other *Pinus* species via an inertia effect (55, 56). When removing the influence of climate in the early growing season in the southwestern United States, the resulting adjusted latewood width has a stronger relationship to monsoon precipitation compared to the unadjusted latewood (55, 56). So far, only unadjusted latewood widths have been used to reconstruct ΣTCP (27, 28). To remove the influence of early growing season climate on latewood width, we regressed earlywood width onto latewood width and retained the residuals for each individual measurement series (55, 56). By adding one to the zero-mean residuals, we produced an adjusted latewood index (LWa) that, like standard ring-width measurements, has a mean of one over the entirety of the time series (55). The sensitivity of *P. palustris* latewood growing on Carolina bay sand rims is related to microtopographic differences (57). Therefore, the sensitivity of individual trees to ΣTCP varies. By calculating LWa at the series level, we can potentially remove some of the influence of landscape position on latewood and better retain the ΣTCP signal (*SI Appendix*, Fig. S5).

ΣTCP Reconstruction. We used a nested principal component (PC) regression (58) to reconstruct regional ΣTCP from our seven LWa chronologies. We first conducted a PC analysis of the seven LWa site chronologies. We retained only the first PC as a predictor, as it was the only PC with an eigenvalue greater than one and consistently explained over ∼80% of the variance in the LWa chronologies (*SI Appendix*, Table S2). To account for decreasing sample depth back in time, we used a nested reconstruction approach (59). The first reconstruction nest covers the common period of all chronologies (1880 through 2015). We then dropped the youngest chronology as determined by the expressed population signal (60) (*SI Appendix*, Fig. S3) and reran the PC regression with the remaining chronologies as predictors and instrumental ΣTCP as the predictand. We repeated this process until there was only one chronology remaining. The final reconstruction is the combination of the nested models, with each nested model being calibrated from 1948 to 2015.

To evaluate the reconstruction skill of each nested reconstruction model, we used a standard split-sample calibration and validation approach. We divided the instrumental period into two periods of approximately equal length (1948 through 1978 and 1979 through 2015) to cross-validate the ΣTCP reconstruction model. Model validation was performed over the later period (1979 through 2015), and verification statistics were calculated for the early period. The verification was based on the coefficient of determination (R^2), the Reduction of Error (RE) (61), and the Coefficient of Efficiency (CE) (62). We then reversed the calibration period to the latter half and validated on the early half using the same metrics. Positive RE and CE values indicate adequate skill of the model at predicting ΣTCP through time. We did this validation procedure for each reconstruction nest. The earliest nest (based only on the Lewis Ocean Bay chronology) had low explained variance, and we therefore excluded that nest from the reconstruction. To assess model uncertainty, we show the inner 95% (for each year) of 999 reconstruction replicates derived from a maximum entropy bootstrapping (MEBoot) (63). MEBoot preserves the dependence structure (i.e., the autocorrelation and partial autocorrelation functions) of the time series and does not assume stationarity of the time series.

To examine how the timing of the TCs may have influenced LWa, we examined the month of occurrence for each TC that generated TCP from 1948 to 2015. To better attribute ΣTCP to a specific month, we removed years that did not have TCP and removed years that had TCs from multiple months contributing to the ΣTCP. Using this subset of data, we used an ANOVA with a Tukey honestly significant difference post hoc test to compare the LWa grouped by the month of TC occurrence and found that there were no significant differences between groups (*SI Appendix*, Fig. S2). We also performed an ANOVA on TCP for each month of occurrence and found no significant differences (*SI Appendix*, Fig. S2). It is important to note that the sample size of these groups was relatively small (n ranged from 4 to 13); however, August and September account for over 80% of TC activity in the north Atlantic Basin, which is the peak season for latewood growth. Further, the timing of TC occurrence did not exhibit a trend through time, and every TC that produced >100 mm occurred in August and September, indicating that the timing of TCs had a minimal impact on the interpretation of the reconstruction.

Bias Correction. Because the probability distributions of tree-ring reconstructions often differ from those of instrumental data, especially in the tails, we bias-corrected (29) our ΣTCP reconstruction. We bias-corrected each nested model separately, then combined the bias-corrected values for each nested model to get the final bias-corrected reconstruction of ΣTCP. Bias-correction is used here as a postprocessing procedure, similar to its use with climate model outputs (64). We used quantile mapping with the "RQUANT" method in the qmap package (65) in R (66). RQUANT approximates the quantile–quantile relationship by using local linear regressions on regularly spaced quantiles. The bias of a given quantile in the reconstruction is estimated by calculating the difference between the local regression and the quantile derived from the observations. These different bias estimates for each quantile can then be added to the respective quantiles from the reconstruction. Another benefit of bias-correcting the reconstruction is that we can directly compare the reconstructed ΣTCP values with very recent observations, such as those during 2016, 2017, and 2018, when we do not have well-replicated tree-ring data. Once systematic error within the reconstruction has been reduced, a direct comparison to observed values is more appropriate. Therefore, we include the three most recent years from the instrumental data in the bias-corrected reconstruction of ΣTCP. To determine how the postprocessing bias-correction procedure influenced the reconstruction, we calculated the Nash–Sutcliffe CE to assess overall model error (1948 through 2015) before and after bias-correction. We also examined the ratio of the total error that was systematic or related to bias by calculating the systematic mean square error and dividing it by the total mean square error (29, 67). Kernel density estimates of the probability density functions demonstrate that the bias-corrected reconstruction better matches the empirical distribution of the observed data compared to the uncorrected reconstruction (Fig. 2*D*). The bias-corrected reconstruction also addresses the problem of the reconstruction model producing negative ΣTCP estimates. To assess the bias-corrected reconstruction model uncertainty, we applied the same bias-correction procedure to each of the 999 members of the ensemble from the uncorrected reconstruction derived using MEBoot. We then estimated the percentiles for the 95% CIs from the bias-corrected ensemble. While the fit of each nested model is not included in the calculation of the CIs, the RMSEs for each nest only differ by ∼2 mm. Further, for the majority of the reconstruction (from 1740 onward), the RMSE values for the various nested reconstructions only differ by ∼1 mm. Overall model evaluation statistics are slightly improved by the bias-correction procedure, with calibration CE = 0.255 before versus 0.279 after bias-correction for the most replicated nest. The proportion of total error that was systematic error slightly improved after bias-correction, with 20% of the error being systematic in the original reconstruction and 18% following bias-correction.

Number and Duration of TCs. We used the HURDAT2 data set (1851 through 2018) to determine the number, translation speed, and duration of landfalling TCs in our study area. We tabulated any TC that tracked within 223 km—the average size of the moisture plume from a landfalling TC and the diameter that was used in TCPDat (10)—of the center of our study region to generate a time series of the number of landfalling TCs. We calculated translation speed (14) but only for the portions of the TC tracks that fell within 223 km of our study region. We used the distances between the 6-h locations along each TC track using a great circle arc to calculate translation speed. We then averaged the translation speed for all segments of all TC tracks within 223 km of our study region for each year to generate a time series of seasonal average translation speed of landfalling TCs. To calculate seasonal average TC duration, we summed the number of 6-h periods from HURDAT2 during which a TC was located within 223 km of our study region and then divided it by the number of TCs that were in our study region for a given year. Because translation speed as well as the number of TCs influence ΣTCP, we also summed the number of 6-h periods from HURDAT2 that a TC was located within 223 km of our study region for each year to create a time series of seasonal total TC duration that combines the number of TC and the speed of those TCs. We then use seasonal average translation speed, seasonal average TC duration, and total TC duration to examine the relationship of TC speed and duration with instrumental and reconstructed ΣTCP using Spearman's correlation.

To determine potential relationships between extremes in seasonal average TC durations and ΣTCP, we conducted a series of superposed epoch analyses (SEA). In a first SEA, we used reconstructed extreme (≥95th quantile; $n = 12$) ΣTCP years as event years and seasonal average TC duration as a chronology for the current year and over the previous year and following 5-y lags. We then conducted a second SEA in which we used extremes (≥95th quantile; $n = 12$) in seasonal average TC duration as event years and reconstructed ΣTCP as the chronology. We then repeated the same procedure (creating two more SEAs) but replaced seasonal average TC duration with the seasonal average TC translation speed. For the SEA using transition speed as the event series, we had to use the 90th quantile to reach a number of events high enough for the analysis ($n = 11$). All SEAs were conducted for the common period (1851 through 2015). We used 1,000 Monte Carlo simulations to develop bootstrapped CIs to determine statistical significance.

To examine the relationship between TCP and TC speed for individual storms, we computed the TCP per TC and the translation speed per TC. We calculated the TCP for each storm by first summing the daily values of TCP for those days that a storm impacted our study region (from TCPDat) for each of the 43 contiguous grid points used in the ΣTCP reconstruction (Fig. 1). We then averaged the TCP data across the 43 grid points to obtain a regional TCP estimate for a given storm. We calculated translation speed per TC for the portions of the TC tracks that fell within 223 km of our study region, but we averaged the speeds for each storm instead of averaging for the entire season as was done for the seasonal average TC translation speed. We then used Spearman's correlation to calculate the correlation between TCP and translation speed per TC. Lastly, we binned individual TCs in groups that had similar speeds (5-kn groups). For each group that had a sample size of ∼20 or more TCs (5 to 9 kn, 10 to 14 kn, and 15 to 19 kn), we tested for trends in TCP per TC with a Mann–Kendall trend test with Sen's slope using the "MannKendall" function in the R package "Kendall" (68). We then tested for trends in TCP per TC for all individual TCs that influenced our study region to determine whether trends in TCP were related to the translation speeds of TCs.

Trend Analysis. To quantify trends in extremes of reconstructed ΣTCP over time, we use quantile regression (69), using R package "quantreg" (70), to estimate the slope of a regression using time as the predictor and ΣTCP as the response. Whereas ordinary least squares (OLS) regression provides an estimate of the conditional mean (i.e., an estimate of the mean ΣTCP for a given year), quantile regression provides trend estimates for ΣTCP across the full probability distribution. Quantile regression is formulated as an optimization problem that estimates the conditional quantiles by minimizing the sum of absolute errors that are weighted according to their quantile position (i.e., it does not partition the data into quantiles and then estimate parameters). Here, we estimate the linear relationship between quantiles of ΣTCP and time for quantiles ranging from 0.01 to 0.99. Given that we are particularly interested in changes in extreme ΣTCP, we focus on trends in the upper tail of the distribution, such as the 0.95 quantile and higher, and compare them to trends in the center of the distribution (Fig. 3). Like OLS, quantile regression provides estimates of the uncertainty of different quantiles. In our application (using a zero-limited variable), the higher quantiles clearly have higher uncertainties compared to the lower quantiles (Fig. 3*B*). We used the "rank" method to determine the 95% CI around each quantile regression slope. While our bias-correction procedure did not inflate the variance during the instrumental period (variance of 5,162.3 in the original reconstruction compared to 5,271.7 in the bias-corrected reconstruction), bias-correction increased the variance during the preinstrumental period, with the variance being 43% higher over the full reconstruction in the bias-corrected time series. The estimates of uncertainty that are derived from the quantile regression trends (Fig. 3) became larger after bias-correction. As a result, the changes in uncertainty that come from the distribution-altering properties of bias-correction are, to a large extent, captured in the quantile regression-based trend estimates. To determine whether the annual number, the seasonal average duration, and the seasonal average translation speed of TCs (1851 through 2018) showed a significant trend, we used a Mann–Kendall trend test with Sen's slope using the "MannKendall" function in the R package "Kendall" (68).

Large-Scale Climate Drivers. To determine the role of large-scale atmospheric-oceanic modes of variability on ΣTCP variability, we compiled climate indices with a well-known influence on TC genesis, development, and tracks. Specifically, we used the bivariate ENSO index (BEST) (71) time series (June through November; 1950 through 2016) from the National Oceanic and Atmospheric Administration Physical Science Laboratory. We also used the summer North Atlantic Oscillation index (NAO; 1948 through 2018) (72) and June through November averages of the Atlantic Multidecadal Oscillation (AMO; 1856 through 2018) (73) and the Bermuda High Index (1948 through 2018) (74, 75). Lastly, we gathered gridded SSTs for the North Atlantic from the Hadley Center (76) for the period 1850 through 2016. We then calculated Pearson correlation coefficients between all climate drivers and the ΣTCP reconstruction over their period of overlap. To compare over the full reconstruction period, we also compared our ΣTCP reconstruction with AMO (May through September) (77) (annual) (78), NAO (winter) (79, 80), NAO (summer) (81), ENSO (annual) (82) (winter) (83), and tropical North Atlantic SSTs (April through March tropical year) (36) reconstructions.

Data Availability. All data and code can be accessed in the supplemental files. Raw tree-ring chronologies and the reconstruction from this paper is archived at the International Tree-Ring Data Bank (https://www.ncdc.noaa.gov/data-access/paleoclimatology-data/datasets/tree-ring) in additon to being available in the supplemental files. All data are included in the article and/or supporting information.

ACKNOWLEDGMENTS. We thank Julia Adams, Tsun Fung Au, Briana Hibner, April Kaiser, Andrew Matej, Tyler Mitchell, Evan Montpellier, Thomas Patterson, Brandon Strange, and Jeffy Summers for help in the field and laboratory. This research was supported by funding from the NSF Grants GSS-1660432 and AGS-210288.

1. R. A. Pielke *et al*., Normalized hurricane damage in the United States: 1900–2005. *Nat. Hazards Rev.* **9**, 29–42 (2008).
2. NOAA National Centers For Environmental Information, U.S. billion-dollar weather and climate disasters, 1980 - present (NCEI Accession 0209268) (2020). https://doi.org/10.25921/STKW-7W73 (28 January 2021).
3. E. N. Rappaport, Loss of life in the United States associated with recent Atlantic tropical cyclones. *Bull. Am. Meteorol. Soc.* **81**, 2065–2074 (2000).
4. E. N. Rappaport, Fatalities in the United States from Atlantic tropical cyclones: New data and interpretation. *Bull. Am. Meteorol. Soc.* **95**, 341–346 (2014).
5. T. R. Knutson *et al*., Tropical cyclones and climate change. *Nat. Geosci.* **3**, 157–163 (2010).
6. H.-S. Kim *et al*., Tropical cyclone simulation and response to CO2 doubling in the GFDL CM2.5 high-resolution coupled climate model. *J. Clim.* **27**, 8034–8054 (2014).
7. M. D. Risser, M. F. Wehner, Attributable human-induced changes in the likelihood and magnitude of the observed extreme precipitation during Hurricane Harvey. *Geophys. Res. Lett.* **44**, 12457–12464 (2017).
8. G. J. van Oldenborgh *et al*., Attribution of extreme rainfall from Hurricane Harvey, August 2017. *Environ. Res. Lett.* **12**, 124009 (2017).
9. T. Knutson *et al*., Tropical cyclones and climate change assessment: Part II: Projected response to anthropogenic warming. *Bull. Am. Meteorol. Soc.* **101**, E303–E322 (2020).
10. J. C. Bregy *et al*., Spatiotemporal variability of tropical cyclone precipitation using a high-resolution, gridded (0.25° × 0.25°) dataset for the eastern United States, 1948–2015. *J. Clim.* **33**, 1803–1819 (2020).
11. C. W. Landsea, Meteorology: Hurricanes and global warming. *Nature* **438**, E11–E12, discussion E13 (2005).
12. C. W. Landsea, G. A. Vecchi, L. Bengtsson, T. R. Knutson, Impact of duration thresholds on Atlantic tropical cyclone counts. *J. Clim.* **23**, 2508–2519 (2010).
13. P. J. Klotzbach, S. G. Bowen, R. Pielke, M. Bell, U. S. Continental, Hurricane landfall frequency and associated damage: Observations and future risks. *Bull. Am. Meteorol. Soc.* **99**, 1359–1376 (2018).

14. J. P. Kossin, A global slowdown of tropical-cyclone translation speed. *Nature* **558**, 104–107 (2018).
15. T. M. Hall, J. P. Kossin, Hurricane stalling along the North American coast and implications for rainfall. *npj Clim. Atmos. Sci.* **2**, 1–9 (2019).
16. J. P. Kossin, Reply to: Moon, I.-J. et al.; Lanzante, J. R. *Nature* **570**, E16–E22 (2019).
17. G. A. Vecchi *et al*., Weakening of tropical Pacific atmospheric circulation due to anthropogenic forcing. *Nature* **441**, 73–76 (2006).
18. D. Coumou, J. Lehmann, J. Beckmann, Climate change. The weakening summer circulation in the Northern Hemisphere mid-latitudes. *Science* **348**, 324–327 (2015).
19. K. T. F. Chan, Are global tropical cyclones moving slower in a warming climate? *Environ. Res. Lett.* **14**, 104015 (2019).
20. J. R. Lanzante, Uncertainties in tropical-cyclone translation speed. *Nature* **570**, E6–E15 (2019).
21. I.-J. Moon, S.-H. Kim, J. C. L. Chan, Climate change and tropical cyclone trend. *Nature* **570**, E3–E5 (2019).
22. T. C. Peterson *et al*., Changes in weather and climate extremes: State of knowledge relevant to air and water quality in the United States. *J. Air Waste Manag. Assoc.* **64**, 184–197 (2014).
23. K. Walsh, Fine resolution simulations of the effect of climate change on tropical cyclones in the South Pacific. *Clim. Dyn.* **45**, 2619–2631 (2015).
24. J. T. Maxwell, P. A. Knapp, J. T. Ortegren, D. L. Ficklin, P. T. Soulé, Changes in the mechanisms causing rapid drought cessation in the southeastern United States. *Geophys. Res. Lett.* **44**, 12,476–12,483 (2017).
25. J. T. Maxwell, J. T. Ortegren, P. A. Knapp, P. T. Soulé, Tropical cyclones and drought amelioration in the gulf and southeastern coastal United States. *J. Clim.* **26**, 8440–8452 (2013).
26. K. E. Kunkel *et al*., Recent increases in U.S. heavy precipitation associated with tropical cyclones. *Geophys. Res. Lett.* **37**, L24706 (2010).
27. P. A. Knapp, J. T. Maxwell, P. T. Soulé, Tropical cyclone rainfall variability in coastal North Carolina derived from longleaf pine (Pinus palustris Mill.): AD 1771-2014. *Clim. Change* **135**, 311–323 (2016).
28. P. A. Knapp, P. T. Soulé, J. T. Maxwell, J. T. Ortegren, T. J. Mitchell, Tropical cyclone precipitation regimes since 1750 and the great suppression of 1843–1876 along coastal North Carolina, USA. *Int. J. Climatol.* **41**, 200–210 (2021).
29. S. M. Robeson, J. T. Maxwell, D. L. Ficklin, Bias-correction of Paleoclimatic reconstructions: A new look at 1,200+ years of Upper Colorado River flow. *Geophys. Res. Lett.* **47**, e2019GL086689 (2020).
30. US Department of Commerce, Hurricane Florence: September 14, 2018. https://www.weather.gov/ilm/HurricaneFlorence.
31. US Department of Commerce, Hurricane Matthew in the Carolinas: October 8, 2016. https://www.weather.gov/ilm/Matthew.
32. D. M. Ludlum, *Early American Hurricanes, 1492-1870* (American Meteorological Society, Boston, c1963).
33. C. W. Landsea, J. L. Franklin, Atlantic hurricane database uncertainty and presentation of a new database format. *Mon. Weather Rev.* **141**, 3576–3592 (2013).
34. R. C. Nogueira, B. D. Keim, D. P. Brown, K. D. Robbins, Variability of rainfall from tropical cyclones in the eastern USA and its association to the AMO and ENSO. *Theor. Appl. Climatol.* **112**, 273–283 (2013).
35. M. A. Saunders, A. S. Lea, Large contribution of sea surface warming to recent increase in Atlantic hurricane activity. *Nature* **451**, 557–560 (2008).
36. J. E. Tierney *et al*., Tropical sea surface temperatures for the past four centuries reconstructed from coral archives. *Paleoceanography* **30**, 226–252 (2015).
37. T. R. Knutson *et al*., Dynamical downscaling projections of twenty-first-century Atlantic hurricane activity: CMIP3 and CMIP5 model-based scenarios. *J. Clim.* **26**, 6591–6617 (2013).
38. E. D. Gutmann *et al*., Changes in hurricanes from a 13-yr convection-permitting pseudo–global warming simulation. *J. Clim.* **31**, 3643–3657 (2018).
39. L. Li, P. Chakraborty, Slower decay of landfalling hurricanes in a warming world. *Nature* **587**, 230–234 (2020).
40. S. Wang, R. Toumi, Recent migration of tropical cyclones toward coasts. *Science* **371**, 514–517 (2021).
41. S. J. Camargo, A. A. Wing, Increased tropical cyclone risk to coasts. *Science* **371**, 458–459 (2021).
42. T. M. Hall, J. P. Kossin, T. Thompson, T. McMahon, US tropical cyclone activity in the 2030s based on projected changes in tropical sea surface temperature. *J. Clim.* **34**, 1321–1335 (2021).
43. C. Setzer, M. E. Domino, Medicaid outpatient utilization for waterborne pathogenic illness following Hurricane Floyd. *Public Health Rep.* **119**, 472–478 (2004).
44. K. A. Novick *et al*., The increasing importance of atmospheric demand for ecosystem water and carbon fluxes. *Nat. Clim. Chang.* **6**, 1023–1027 (2016).
45. K. E. Trenberth, A. Dai, R. M. Rasmussen, D. B. Parsons, The changing character of precipitation. *Bull. Am. Meteorol. Soc.* **84**, 1205–1218 (2003).
46. P. A. O'Gorman, T. Schneider, The physical basis for increases in precipitation extremes in simulations of 21st-century climate change. *Proc. Natl. Acad. Sci. U.S.A.* **106**, 14773–14777 (2009).
47. N. Ban, J. Schmidli, C. Schär, Heavy precipitation in a changing climate: Does short-term summer precipitation increase faster? *Geophys. Res. Lett.* **42**, 1165–1172 (2015).
48. R. W. Higgins, A. Leetmaa, Y. Xue, A. Barnston, Dominant factors influencing the seasonal predictability of U.S. precipitation and surface air temperature. *J. Clim.* **13**, 3994–4017 (2000).
49. K. R. Knapp, M. C. Kruk, D. H. Levinson, H. J. Diamond, C. J. Neumann, The international best track archive for climate stewardship (IBTrACS): Unifying tropical cyclone data. *Bull. Am. Meteorol. Soc.* **91**, 363–376 (2010).
50. J. E. Lodewick, No. 5 effect of certain climatic factors on the diameter growth of longleaf pine in western Florida. *J. Agric. Res.* **41**, 349 (1930).
51. R. L. Holmes, *Program COFECHA User's Manual. Laboratory of Tree-Ring Research* (The University of Arizona, Tucson, 1983).
52. E. R. Cook, K. Peters, The smoothing spline: A new approach to standardizing forest interior tree-ring width series for dendroclimatic studies. *Tree-Ring Bulletin* **41**, 45–53 (1981).
53. N. W. Bussberg, J. T. Maxwell, S. M. Robeson, C. Huang, The effect of end-point adjustments on smoothing splines used for tree-ring standardization. *Dendrochronologia* **60**, 125665 (2020).
54. E. R. Cook, "A time-series analysis approach to tree-ring standardization," PhD dissertation, The University of Arizona Press, Tucson (1985).
55. D. M. Meko, C. H. Baisan, Pilot study of latewood-width of conifers as an indicator of variability of summer rainfall in the North American monsoon region. *Int. J. Climatol.* **21**, 697–708 (2001).
56. D. Griffin *et al*., North American monsoon precipitation reconstructed from tree-ring latewood. *Geophys. Res. Lett.* **40**, 954–958 (2013).
57. E. E. Montpellier, P. A. Knapp, P. T. Soulé, J. T. Maxwell, Microelevational differences affect longleaf pine (Pinus palustris Mill.) sensitivity to tropical cyclone precipitation: A case study using LiDAR. *Tree-Ring Res.* **76**, 89–93 (2020).
58. E. R. Cook *et al*., Old world megadroughts and pluvials during the Common Era. *Sci. Adv.* **1**, e1500561 (2015).
59. D. Meko, Dendroclimatic reconstruction with time varying predictor subsets of tree indices. *J. Clim.* **10**, 687–696 (1997).
60. T. M. L. Wigley, K. R. Briffa, P. D. Jones, On the average value of correlated time series, with applications in dendroclimatology and hydrometeorology. *J. Appl. Meteorol. Climatol.* **23**, 201–213 (1984).
61. H. C. Fritts, *Tree Rings and Climate* (Academic, New York, 1976).
62. J. E. Nash, J. V. Sutcliffe, River flow forecasting through conceptual models. Part I — A discussion of principles. *J. Hydrol. (Amst.)* **10**, 282–290 (1970).
63. H. D. Vinod, Maximum entropy ensembles for time series inference in economics. *J. Asian Econ.* **17**, 955–978 (2006).
64. D. L. Ficklin, J. T. Abatzoglou, S. M. Robeson, A. Dufficy, The influence of climate model biases on projections of aridity and drought. *J. Clim.* **29**, 1269–1285 (2016).
65. L. Gudmundsson, J. B. Bremnes, J. E. Haugen, T. Engen-Skaugen, Technical note: Downscaling RCM precipitation to the station scale using statistical transformations – a comparison of methods. *Hydrol. Earth Syst. Sci.* **16**, 3383–3390 (2012).
66. R Core Team, R: A language and environment for statistical computing. R foundation for statistical computing, Vienna, Austria (2020). https://www.R-project.org/.
67. C. J. Willmott, On the validation of models. *Phys. Geogr.* **2**, 184–194 (1981).
68. A. I. McLeod, Kendall: Kendall rank correlation and Mann-Kendall trend test. R package version 2.2. (2011). https://cran.r-project.org/package/Kendall/index.html.
69. R. Koenker, G. Bassett, Regression quantiles. *Econometrica* **46**, 33–50 (1978).
70. R. Koenker, V. Chernozhukov, X. He, L. Peng, Eds., *Handbook of Quantile Regression* (CRC Press, 2017).
71. C. A. Smith, P. D. Sardeshmukh, The effect of ENSO on the intraseasonal variance of surface temperatures in winter. *Int. J. Climatol.* **20**, 1543–1557 (2000).
72. J. Li, J. X. L. Wang, A modified zonal index and its physical sense. *Geophys. Res. Lett.* **30**, 1632 (2003).
73. D. B. Enfield, A. M. Mestas-Nuñez, P. J. Trimble, The Atlantic multidecadal oscillation and its relation to rainfall and river flows in the continental U.S. *Geophys. Res. Lett.* **28**, 2077–2080 (2001).
74. D. W. Stahle, M. K. Cleaveland, Reconstruction and analysis of spring rainfall over the southeastern U.S. for the past 1000 years. *Bull. Am. Meteorol. Soc.* **73**, 1947–1961 (1992).
75. J. T. Ortegren, P. A. Knapp, J. T. Maxwell, W. P. Tyminski, P. T. Soulé, Ocean–atmosphere influences on low-frequency warm-season drought variability in the Gulf Coast and Southeastern United States. *J. Appl. Meteorol. Climatol.* **50**, 1177–1186 (2011).
76. N. A. Rayner *et al*., Global analyses of sea surface temperature, sea ice, and night marine air temperature since the late nineteenth century. *J. Geophys. Res. D Atmos.* **108**, 4407 (2003).
77. S. T. Gray, L. J. Graumlich, J. L. Betancourt, G. T. Pederson, A tree-ring based reconstruction of the Atlantic multidecadal oscillation since 1567 A.D. *Geophys. Res. Lett.* **31**, L12205 (2004).
78. J. Wang *et al*., Internal and external forcing of multidecadal Atlantic climate variability over the past 1,200 years. *Nat. Geosci.* **10**, 512–517 (2017).
79. E. R. Cook *et al*., A Euro-Mediterranean tree-ring reconstruction of the winter NAO index since 910 C.E. *Clim. Dyn.* **53**, 1567–1580 (2019).
80. V. Trouet *et al*., Persistent positive North Atlantic oscillation mode dominated the Medieval climate anomaly. *Science* **324**, 78–80 (2009).
81. C. K. Folland *et al*., The summer North Atlantic oscillation: Past, present, and future. *J. Clim.* **22**, 1082–1103 (2009).
82. K. Braganza, J. L. Gergis, S. B. Power, J. S. Risbey, A. M. Fowler, A multiproxy index of the El Niño–Southern oscillation, A.D. 1525–1982. *J. Geophys. Res. D Atmos.* **114**, D05106 (2009).
83. J. Li *et al*., El Niño modulations over the past seven centuries. *Nat. Clim. Chang.* **3**, 822–826 (2013).